

Braiding Majorana Zero Modes through high frequency virtual tunneling

Pranay Gorantla and Rajdeep Sensarma

Department of Theoretical Physics, Tata Institute of Fundamental Research, Mumbai 400005, India.

Braiding of non-Abelian Majorana anyons is a first step towards using them in quantum computing. We propose a new protocol for braiding Majorana zero modes formed at the edges of nanowires with strong spin orbit coupling and proximity induced superconductivity. Our protocol uses high frequency virtual tunneling between the ends of the nanowires in a tri-junction, which lead to an effective low frequency coarse grained dynamics for the system, to perform the braid. The braiding operation is immune to amplitude noises in the drives, and depends on relative phase between two drives, which can be controlled by usual phase locking techniques. We also show how our proposal can be scaled to a network of qubits using a honeycomb lattice geometry.

Gapped two dimensional quantum many body systems can sustain localized excitations (anyons) which have non-Abelian mutual statistics [1–3]. The result of moving a non-Abelian anyon around another does not result in the multiplication of the wavefunction by ± 1 (bosons/fermions), or by a phase (Abelian anyons [4, 5]); rather it generates a non-trivial unitary rotation in a degenerate subspace of the system. This process, called braiding of anyons [6], is immune to local perturbations, provided the process is carried out adiabatically. Braiding of anyons is a key step towards achieving fault tolerant quantum gates, which are the building blocks of an architecture for fault tolerant quantum computing [3, 7–9].

Non-Abelian anyonic excitations arise either in cores of topological defects in either symmetry-broken or ordered states [10], or as localized excitations in strongly interacting systems [11]. A promising candidate for experimental realization and manipulation of anyons are the localized Majorana modes in semiconductor-superconductor heterostructures with strong spin orbit coupling [12–17]. While there are several proposals [12–15] to realize these excitations, in recent years, localized Majorana modes have been experimentally realized [18–29] at the end points of semiconductor nanowires with strong spin orbit coupling and proximity induced superconductivity.

The Majorana nanowires are described by a topologically equivalent one dimensional Kitaev model [30], which can be driven to a “topological phase,” where the ground state has topological zero-energy edge modes by careful tuning of band structure and chemical potential in the system. The Kitaev chain is best described by writing the electron operators at each lattice site in terms of two Majorana operators. In the topological phase, the Majorana operators on nearest neighbours are paired, leaving an unpaired Majorana mode at each end at exactly zero energy, the so called Majorana zero mode (MZM). In a long wire, these states are robust to local perturbations, and are protected by the pairing gap of the other Majorana degrees of freedom [10, 30, 31]. A pair of Majorana operators can be linearly combined to form a single complex fermion, creating a two dimensional degenerate subspace corresponding to the presence/absence of this fermion. The braid operation then creates a unitary rotation by $\pi/2$ in this subspace [6].

Several proposals exist in the literature for braiding of MZMs [32–38]. Most proposals require a tri-junction of three Majorana nanowires, which represent the simplest 2D network of Kitaev chains [36], while proposals with larger number of nanowires [39] have also been proposed. More recent proposals have used a “shortcut to adiabaticity” approach to achieve braiding of MZMs [38]. The tri-junction can host unpaired Majorana modes at 4 possible positions, three at the ends of the wires far from each other, and one at the junction. In the initial and final state, two of the wires are in the topological phase, with the MZMs at their endpoints forming the qubit. The braiding sequence involves driving different wires in and out of topological phases [36] to move one MZM around the other.

In this Letter, we propose a new protocol for braiding MZMs using a sequence of high frequency tunneling drives between the end-sites of the Majorana nanowires, together with three ancilliary Majorana operators which are not part of the qubit. The frequencies are detuned from the pairing gap, leading to an effective slow non-dissipative dynamics in the system, which can be treated within a high frequency expansion. This effective dynamics generates the braiding of the MZMs. A key feature of this protocol is that braiding is completely immune to amplitude noise in the drives. The protocol depends only on the phase difference between the drives, which allows the protocol to be operated at low phase noise by locking the phase of the drives. Finally we show that the protocol can be scaled by constructing a honeycomb lattice of the wires, leading to a network of such qubits in a two-dimensional geometry.

The key building block of our proposal to braid Majorana fermions is a protocol to adiabatically drive the coupling between two Majorana operators by coupling each of them to a third Majorana operator with high frequency drives. This process is shown in Fig 1(a), where $\gamma_{x/y/z}$ are three Majorana operators at the end of three nanowires. We drive the coupling (tunneling) between γ_x and γ_y with a frequency $\bar{\omega}$, an amplitude \bar{h} , and a phase $\bar{\phi}$, shown by the dashed red line. Simultaneously, we also drive a tunneling between γ_x and γ_z with a frequency ω , an amplitude h , and a phase ϕ , shown by the dotted blue line. If the protocol is arranged such that $|\Delta\omega| = |\omega - \bar{\omega}|, h, \bar{h} \ll \omega, \bar{\omega}$, the separation of scales leads

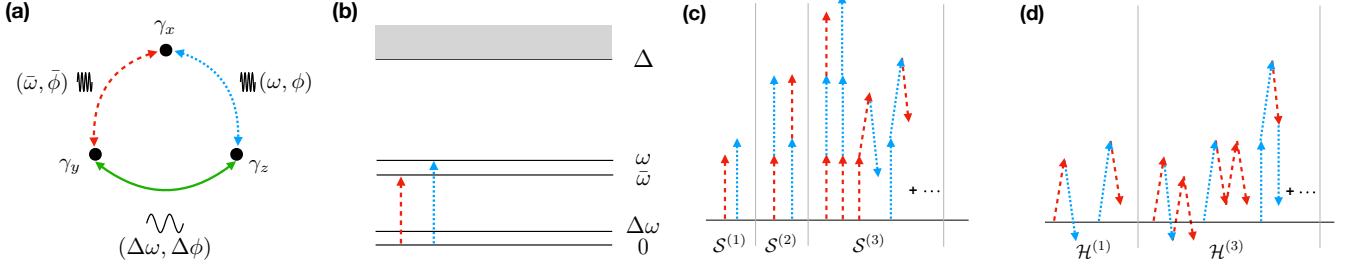


FIG. 1. (a) The building block of our protocol. The arrowed lines represent the tunnelings between Majorana operators: dashed red and dotted blue lines are the high frequency drives, and solid green line is the effective low frequency coupling. (b) Typical frequency and energy scales in the problem. Δ is the semiconducting gap in the nanowire which sets the highest scale. The dashed red and dotted blue arrows have drive frequencies which are chosen to lie deep inside the gap, $\omega, \bar{\omega} \ll \Delta$, and to have a very small difference, $\Delta\omega \ll \omega, \bar{\omega}$. The energy differences are exaggerated for illustration. (c) Some representative terms in $\mathcal{S}^{(1)}$, $\mathcal{S}^{(2)}$ and $\mathcal{S}^{(3)}$ with frequencies $\sim \omega$ or higher. (d) Some representative terms in $\mathcal{H}^{(1)}$ and $\mathcal{H}^{(3)}$ with frequencies $\sim \Delta\omega$. For each sequence to end near 0, we require even number of drive terms (red and blue arrows) which is possible only at odd orders.

to an effective description of the dynamics of the system on a scale $\sim 1/\Delta\omega$, obtained by a high frequency expansion, which coarse grains the dynamics on a scale $\sim 1/\omega$. We note that $\omega, \bar{\omega}$ must be far detuned from the superconducting gap Δ , so that the system does not absorb and make transitions. Fig. 1(b) shows a schematic of the energy scales involved in the process with $|\Delta\omega| \ll \omega, \bar{\omega} \ll \Delta$. For experimentally observed $\Delta \sim 60$ GHz [20], the choice of parameters $\omega, \bar{\omega} \sim 1 - 5$ GHz, with $h, \bar{h}, \Delta\omega \sim 50$ MHz is reasonable and feasible [40]. The key result, which we will elaborate below, is that in the coarse-grained description, (γ_x, γ_y) and (γ_x, γ_z) are decoupled, while (γ_y, γ_z) are coupled by an effective drive of amplitude $\sim h^2/\omega$, modulated at multiples of $\Delta\omega$, with phase $\sim \phi - \bar{\phi}$, as shown by the solid green line in Fig 1(a).

The Hamiltonian which drives (γ_x, γ_y) and (γ_x, γ_z) is given by

$$H(t) = \bar{h} \sin(\bar{\omega}t + \bar{\phi}) i\gamma_x \gamma_y + h \sin(\omega t + \phi) i\gamma_z \gamma_x. \quad (1)$$

In the high frequency expansion, the inverse propagator $G^{-1} = i\partial_t - H(t)$ is transformed by a unitary operator $e^{-i\mathcal{S}(t)}$ to $\mathcal{G}^{-1} = e^{i\mathcal{S}(t)} G^{-1} e^{-i\mathcal{S}(t)} = i\partial_t - \mathcal{H}(t)$. Using $[i\mathcal{S}, i\partial_t] = \dot{\mathcal{S}}$, we get

$$\mathcal{H} = \sum_{m=0}^{\infty} \frac{1}{m!} \left[i\mathcal{S}, \left[i\mathcal{S}, \dots \left[i\mathcal{S}, H - \frac{\dot{\mathcal{S}}}{m+1} \right] \dots \right] \right]. \quad (2)$$

Here, \mathcal{S} and, consequently, \mathcal{H} have high frequency expansions, i.e. $\mathcal{S} = \sum_{n=1}^{\infty} \mathcal{S}^{(n)}(t)$ and $\mathcal{H} = \sum_{n=0}^{\infty} \mathcal{H}^{(n)}(t)$, where $\mathcal{S}^{(n)} \sim (h/\omega)^n$ and $\mathcal{H}^{(n)}(t) \sim h^{n+1}/\omega^n$. At each order, $\mathcal{S}^{(n+1)}$ is determined in such a way that $\mathcal{H}^{(n)}$ has only low frequency terms [static or $\mathcal{O}(\Delta\omega)$], while \mathcal{S} contains only high frequency terms $\sim \omega$ or higher harmonics. Some representative terms for $\mathcal{S}^{(1)}$, $\mathcal{S}^{(2)}$, and $\mathcal{S}^{(3)}$ are schematically shown in Fig. 1(c). Each term in the figure is a sequence of red and blue arrows which correspond to drive terms with frequencies $\bar{\omega}$ and ω respectively. Every sequence starts at the baseline, which is the 0 level of frequency, and ends at the

level which corresponds to frequency with which that term is modulated. For example, the first term in $\mathcal{S}^{(2)}$ has a frequency $\omega + \bar{\omega}$, and the third term in $\mathcal{S}^{(3)}$ has a frequency $2\bar{\omega} - \omega$. Since \mathcal{S} can have only high frequency terms, all the sequences must end at a level $\sim \omega$ or higher. The effective low frequency Hamiltonian \mathcal{H} then consists of terms with frequencies $\sim \Delta\omega$, some of which are shown in Fig. 1(d). Unlike \mathcal{S} , the sequences of \mathcal{H} must all end near 0, i.e., $\mathcal{O}(\Delta\omega)$. It is clear that an even number of red and blue arrows are required to bring the sequence to this level, and hence $\mathcal{H}^{(n)}$ is non-zero only for odd n . At order $2p+1$ (p is non-negative integer), $\mathcal{H}^{(2p+1)}$ is a product of terms $\sim (\gamma_x \gamma_y)^k (\gamma_x \gamma_z)^{2p+2-k} \sim \gamma_y^k \gamma_z^{2p+2-k}$, where we have used $\gamma_x^2 = 1$. This is either $\sim \gamma_y \gamma_z$ for odd k or ~ 1 for even k . The Clifford algebra of the Majorana operators, $\{\gamma_\alpha, \gamma_\beta\} = 2\delta_{\alpha\beta}$ and $\gamma_\alpha^\dagger = \gamma_\alpha$ for $\alpha, \beta = x, y, z$, leads to a closed $\mathfrak{so}(3)$ algebra of the bilinears $\gamma_\alpha \gamma_\beta$, with $\alpha \neq \beta$. This, together with the nested commutator form in Eq. 2, implies that identity 1 does not appear in this expansion, i.e., only odd k terms appear and hence all the terms in the effective Hamiltonian obtained at different orders of high frequency expansion are proportional to $\gamma_y \gamma_z$.

Here we quote the effective Hamiltonian for the three Majorana operators upto leading order $\mathcal{O}(h^2/\omega)$ in the high frequency expansion, and refer the reader to Supplementary Material for the next leading order $\mathcal{O}(h^4/\omega^3)$. To $\mathcal{O}(h^2/\omega)$, we have

$$\begin{aligned} \mathcal{S}^{(1)}(t) &= -\frac{\bar{h}}{\bar{\omega}} \cos(\bar{\omega}t + \bar{\phi}) i\gamma_x \gamma_y - \frac{h}{\omega} \cos(\omega t + \phi) i\gamma_z \gamma_x, \\ \mathcal{S}^{(2)}(t) &= -\frac{h\bar{h}}{2\omega\bar{\omega}} \left(\frac{\Delta\omega}{\omega + \bar{\omega}} \right) \cos[(\omega + \bar{\omega})t + \phi + \bar{\phi}] i\gamma_y \gamma_z, \\ \mathcal{H}^{(1)}(t) &= \frac{h\bar{h}}{2\omega\bar{\omega}} (\omega + \bar{\omega}) \sin(\Delta\omega t + \Delta\phi) i\gamma_y \gamma_z. \end{aligned} \quad (3)$$

where $\Delta\phi = \phi - \bar{\phi}$. At higher orders, the only terms in \mathcal{H} are $\sim \sin[k(\Delta\omega t + \Delta\phi)]$ with odd k because, as explained before, only odd k terms appear in the series expansion of \mathcal{H} . There are no terms $\sim \cos[k(\Delta\omega t + \Delta\phi)]$ because in the limit $\omega \rightarrow \bar{\omega}$ and $\phi \rightarrow \bar{\phi}$, the nested commutator in Eq. 2 forces \mathcal{H} to 0. The

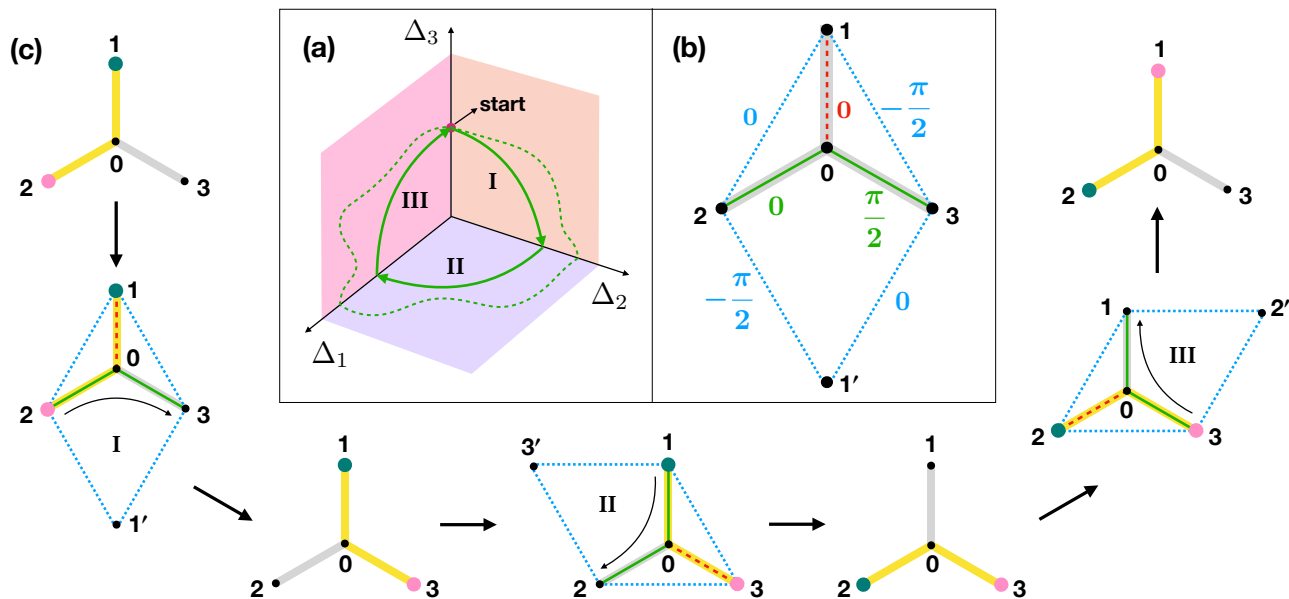


FIG. 2. (a) The solid green curve is one possible path for braiding in the parameter space of Δ_1 , Δ_2 and Δ_3 which subtends a solid angle of $\pi/2$ at the origin. A smooth deformation of the each path segment within the corresponding plane (shown as dashed green line) still subtends the same solid angle. (b) The basic setup containing three wires (gray segments) meeting at a junction with Majorana operators 1, 2, 3 at the ends and 0 at the junction. An additional operator 1' is placed for reasons explained in the text. Like before, the dashed red and dotted blue lines correspond to drives with frequencies $\bar{\omega}$ and ω respectively, and with respective phases shown. The solid green lines represent the effective low frequency couplings. The relative phases tell us this represents step I of the path of our protocol. (c) The three steps of braiding. The yellow segments are in topological phase and the gray segments are in trivial phase. Initially, the unpaired Majorana modes [cyan (dark) and pink (light) big dots], are at 1 and 2 respectively. The setup of (b) is used to perform the three steps, I, II and III, of braiding after which the cyan and pink Majorana modes end up at 2 and 1 respectively. The result is an anticlockwise braiding.

effective Hamiltonian is thus modulated with the beating frequency and its odd harmonics, and a phase which can be controlled by the phase difference between the two drives. This tunable effective Hamiltonian will be the basic building block of our protocol to braid the Majorana modes.

We now describe the detailed protocol to braid Majorana fermions using high frequency tunneling. The basic setup consists of four Majorana fermions at the end of three wires (gray segments), as indicated by the operators 0, 1, 2 and 3 in Fig. 2(b). The different wires can be driven into topological or non-topological phases by changing the coupling Δ_i between the central Majorana operator γ_0 and the operator γ_i . Such coupling can be obtained by modulating the chemical potential in the corresponding wire [36]. In fact a Majorana mode can be transferred from one end to another by suitable tuning of the couplings [36]. The braiding operation can then be represented as a closed path traversed by the system in the parameter space of Δ_1 , Δ_2 and Δ_3 [41]. Two possible paths are shown in Fig. 2(a). We will consider the solid green path. Starting from the point shown in figure, the solid green path consists of three segments in the orthogonal planes $\Delta_2 - \Delta_3$, $\Delta_1 - \Delta_2$ and $\Delta_3 - \Delta_1$, traversed in the sequence shown in the figure, leading to an anticlockwise braiding of Majoranas modes at γ_1 and γ_2 . The braiding operator for this path is $\exp(-\pi\gamma_1\gamma_2/4)$, where $\pi/4$ is the Berry phase which is half the solid angle, $\pi/2$, subtended by the path at origin.

Let us consider the segment labeled I in Fig. 2(a). This requires the coupling between γ_0 and γ_2 to be tuned from zero to a finite value, while at the same time, the coupling between γ_0 and γ_3 is tuned from a finite value to zero. An adiabatic passage along this path would shift the Majorana mode γ_2 to the position shown by γ_3 , as shown in Fig. 2(c). In order to achieve this, we put a high frequency drive between the Majorana operators γ_0 and γ_1 with a frequency $\bar{\omega}$. Simultaneously, we consider a drive with frequency ω between γ_1 and γ_2 , which is phase locked with the drive between γ_0 and γ_1 . Such a drive between Majorana operators at end points of different wires can be obtained by coupling these end points to a common quantum dot [38, 42]. We will denote this common phase to be 0 and measure phases of all other drives with respect to this common phase. We now add another drive between γ_1 and γ_3 with frequency ω and a phase shift of $-\pi/2$. This is depicted in Fig. 2(b), where the dashed red line represents drive with frequency $\bar{\omega}$, while the dotted blue line is a drive with frequency ω . The relative phases of the drives are also shown in the figure. It is easy to see from Eq. 3 that the drive between operators 0 and 1, combined with the drive between 1 and 2 will lead to an effective coupling between 0 and 2 which is modulated as $\sim \sin \Delta\omega t$. Similar considerations with the drive between 0 and 1, and the drive between 1 and 3, would lead to an effective coupling between 0 and 3 modulated as $\sim \sin(\Delta\omega t + \pi/2) \sim \cos \Delta\omega t$. If the drives are

applied for a time $T = \pi/(2\Delta\omega)$, one can achieve the goal of traversing the path segment *I*, i.e. Δ_2 is driven from zero to a finite value, $\hbar\hbar(\omega + \bar{\omega})/(2\omega\bar{\omega})$, while Δ_3 is simultaneously driven from the same finite value to zero.

The above scheme, however, also leads to a static coupling between the operators γ_2 and γ_3 , with the magnitude $\sim \hbar^2/\omega$, which is similar in magnitude to the couplings Δ_2 and Δ_3 . This would lead to a splitting of these Majorana operators, and the topological protection would be lost. To get rid of this coupling, we put two more high frequency drives, one between γ_2 and an auxiliary Majorana operator $\gamma_{1'}$, and another between γ_3 and $\gamma_{1'}$. We note that $\gamma_{1'}$ is an auxiliary operator, which is not part of the qubit considered here. These two drives are both modulated at frequency ω and have phases $\pi/2$ and 0 respectively. This is shown in Fig. 2(b) by the additional dotted blue lines with their respective phases. This provides an alternate pathway of coupling γ_2 and γ_3 , and the phases have been arranged in such a way that the two pathways of coupling γ_2 and γ_3 , one through $\gamma_{1'}$ and the other through $\gamma_{1'}$, interfere destructively, resulting in no additional coupling between γ_2 and γ_3 . We note that there is a residual coupling between γ_2 and γ_3 , which is $\sim \hbar^4/\omega^3$, much smaller than the scale of Δ_2 or Δ_3 . For realistically achievable values of $\omega \sim 1$ GHz, $\hbar \sim 50$ MHz, the finite value of $\Delta_2(\Delta_3)$ is ~ 2.5 MHz, while the small residual splitting is ~ 625 Hz.

The detailed steps of the full braiding scheme are shown in Fig. 2(c). The left part of the figure corresponds to traversing the path segment **I** in the parameter space, at the end of which the Majorana mode γ_2 has been transferred to the position of the operator γ_3 . The bottom part of the figure corresponds to traversing the path segment **II**. In this case, a high frequency drive with frequency $\bar{\omega}$ couples γ_0 and γ_3 , while there are four drives with frequency ω between (γ_3, γ_1) and $(\gamma_2, \gamma_{3'})$ with phase 0 and between $(\gamma_{3'}, \gamma_1)$ and (γ_2, γ_3) with phase $\pi/2$. Here $\gamma_{3'}$ is an auxiliary Majorana operator which is not part of the qubit. At the end of the sequence, the Majorana mode at γ_1 is moved to the position of γ_2 . The right part of the figure depicts the path segment **III**, which moves the mode at γ_3 to that at γ_1 and uses an auxiliary Majorana operator $\gamma_{2'}$. The full sequence then leads to the braiding of the modes γ_1 and γ_2 in the anticlockwise direction. The reverse sequence of paths would lead to a clockwise braid of the Majoranas.

We will now discuss the robustness of our protocol. First, note that in Fig. 2(a), deforming the solid green path to the dashed green path gives the same Berry phase $\pi/4$ because the three deformed segments also lie in the same orthogonal planes. It is evident that the braiding operation is then protected against any deformation of each segment within the corresponding orthogonal plane, although there is no protection against arbitrary deformation, say, out of the plane. It is also essential that different segments meet exactly along the axes of the parameter space. For example, consider the segments **I** and **II** which ideally meet on the Δ_2 axis. If Δ_3 is not turned off exactly at 0, then the meeting point is not exactly on the Δ_2 axis and the segment **II** will not lie in the plane $\Delta_1 - \Delta_2$, resulting in a solid angle different from $\pi/2$. Hence, every

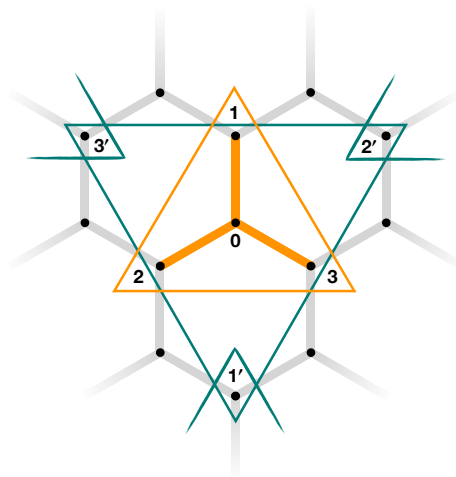


FIG. 3. A qubit+ancillary cell in a honey-comb lattice. The nanowires form the edges of the lattice and the vertices host Majorana modes. The qubit Majorana operators are inside the smaller orange triangle and ancillary Majorana operators are inside the bigger cyan triangle but outside the smaller orange triangle. The orange segments in the centre correspond to the three parameters of braiding. The gray segments are in trivial phase. The ancillary Majorana operators can be shared among adjacent cells provided these qubits are not processed simultaneously.

meeting point must be along the one of the three axes of the parameter space.

In our protocol, the leading order terms in \mathcal{H} clearly satisfy the above criteria. Moreover, even if we consider the higher order terms, it can be shown using a simple algebraic argument that the paths get deformed only within the planes and still meet exactly along the axes (see Supplementary Material for details). So, there is no braiding error from the truncation of the series. Now, we are left with only practical errors like amplitude noise and phase noise in the drives. The amplitude noise has no effect because it only deforms the path within the planes and does not disturb the meeting point of different segments. Phase noise, however, can affect the meeting point and change the Berry phase. Since the phase of the effective Hamiltonian depends only on the difference of phases of the drives, the only noise that can really affect the protocol is the noise in relative phases. For the values of $\omega, \bar{\omega}$ quoted before, it is practically easy to keep the relative phase fixed on time scales $\sim 1/\Delta\omega$ if the drives are obtained by modulating a single source. So, our protocol is also immune to different sources of noise from the drives.

This braiding scheme can be extended to a honey-comb lattice of qubits and ancillaries as shown in Fig. 3. The lattice is made of 1D nanowires and each junction can host an unpaired Majorana mode by driving appropriate wires to topological phases. The four Majorana operators within the smaller orange triangle make up the qubit and the three Majorana operators inside the bigger cyan triangle, but outside the smaller orange triangle, make up the ancillaries. The quantum information is stored in the qubit whereas the ancillaries participate

only in the manipulation of this information through braiding operations. The combined qubit+ancillary cell can then be repeated along the lattice. Notice that adjacent cells can share the ancillaries as shown by partially drawn triangles on three sides, provided these qubits are not processed simultaneously. This architecture is similar in spirit to transistors on a chip. Like the latter, we believe that an efficient packing of the cells by sharing maximum number of ancillaries can be found and leave it for future research.

In this Letter, we propose a new way of braiding MZMs using high frequency virtual tunneling between the ends of Majorana nanowires in a tri-junction. The high frequency drives lead to an effective coarse grained low frequency dynamics, which implements the braiding operation. The protocol is immune to amplitude noise in the drives and depends only on relative phase between drives, which can be controlled using standard phase locking techniques. We also show how we can create a densely packed architecture using a honeycomb lattice of Majorana nanowires.

The authors acknowledge the use of computational facilities at Department of Theoretical Physics, TIFR Mumbai. The authors acknowledge helpful discussions with Bernard van Heck and Jay Deep Sau.

SUPPLEMENTARY MATERIAL

High Frequency Expansion up to $\mathcal{O}(h^4/\omega^3)$

In the main text, we gave the expression for effective Hamiltonian to leading order $\mathcal{O}(h^2/\omega)$ in Eq. 3. Here, we give the derivation of these expressions up to $\mathcal{O}(h^4/\omega^3)$. The original Hamiltonian given in Eq. 1 in the main text is

$$H(t) = \bar{h} \sin(\bar{\omega}t + \bar{\phi}) i\gamma_x \gamma_y + h \sin(\omega t + \phi) i\gamma_z \gamma_x. \quad (4)$$

Using the nested commutator of Eq. (2) in the main text, up to $\mathcal{O}(h)$, we have

$$\mathcal{H}^{(0)} = H - \dot{\mathcal{S}}^{(1)} = \bar{h} \sin(\bar{\omega}t + \bar{\phi}) i\gamma_x \gamma_y + h \sin(\omega t + \phi) i\gamma_z \gamma_x - \dot{\mathcal{S}}^{(1)}. \quad (5)$$

Since both the terms are of high frequency, we choose $\mathcal{S}^{(1)}$ to be

$$\mathcal{S}^{(1)}(t) = -\frac{\bar{h}}{\bar{\omega}} \cos(\bar{\omega}t + \bar{\phi}) i\gamma_x \gamma_y - \frac{h}{\omega} \cos(\omega t + \phi) i\gamma_z \gamma_x. \quad (6)$$

Therefore, to $\mathcal{O}(h)$, the effective Hamiltonian is

$$\mathcal{H}^{(0)}(t) = 0. \quad (7)$$

Similarly, at $\mathcal{O}(h^2/\omega)$, we have

$$\begin{aligned} \mathcal{H}^{(1)} &= \left[i\mathcal{S}^{(1)}, \left(H - \frac{\dot{\mathcal{S}}^{(1)}}{2} \right) \right] - \dot{\mathcal{S}}^{(2)} \\ &= \frac{h\bar{h}}{2\omega\bar{\omega}} (\omega + \bar{\omega}) \sin[(\omega - \bar{\omega})t + \phi - \bar{\phi}] i\gamma_y \gamma_z \\ &\quad + \frac{h\bar{h}}{2\omega\bar{\omega}} (\omega - \bar{\omega}) \sin[(\omega + \bar{\omega})t + \phi + \bar{\phi}] i\gamma_y \gamma_z - \dot{\mathcal{S}}^{(2)}. \end{aligned} \quad (8)$$

To cancel only the high frequency terms, we choose $\mathcal{S}^{(2)}$ to be

$$\mathcal{S}^{(2)}(t) = -\frac{h\bar{h}}{2\omega\bar{\omega}} \left(\frac{\omega - \bar{\omega}}{\omega + \bar{\omega}} \right) \cos[(\omega + \bar{\omega})t + \phi + \bar{\phi}] i\gamma_y \gamma_z \quad (9)$$

Therefore, at $\mathcal{O}(h^2/\omega)$, the effective Hamiltonian is

$$\mathcal{H}^{(1)}(t) = \frac{h\bar{h}}{2\omega\bar{\omega}} (\omega + \bar{\omega}) \sin[(\omega - \bar{\omega})t + \phi - \bar{\phi}] i\gamma_y \gamma_z \quad (10)$$

Combining the above results, the effective Hamiltonian up to $\mathcal{O}(h^2/\omega)$ is

$$\mathcal{H}(t) = \frac{h\bar{h}}{2\omega\bar{\omega}} (\omega + \bar{\omega}) \sin(\Delta\omega t + \Delta\phi) i\gamma_y \gamma_z. \quad (11)$$

As we have shown in main text, $\mathcal{H}^{(n)}$ is non-zero only for odd n . Hence, the next non-zero term in \mathcal{H} comes at third order. Continuing the same procedure, we obtain the following expressions for $\mathcal{S}^{(3)}$, $\mathcal{S}^{(4)}$ and $\mathcal{H}^{(3)}$,

$$\begin{aligned} \mathcal{S}^{(3)}(t) &= \frac{h\bar{h}^2}{12\omega\bar{\omega}^2} \left[\frac{(\omega - \bar{\omega})(\omega - 2\bar{\omega})}{(\omega + \bar{\omega})(\omega + 2\bar{\omega})} \cos[(\omega + 2\bar{\omega})t + \phi + 2\bar{\phi}] + \frac{(5\omega + 11\bar{\omega})}{(\omega + \bar{\omega})} \cos(\omega t + \phi) \right. \\ &\quad \left. + \frac{4(\omega + \bar{\omega})}{(\omega - 2\bar{\omega})} \cos[(2\bar{\omega} - \omega)t + 2\bar{\phi} - \phi] \right] i\gamma_z \gamma_x \\ &\quad + \frac{h^2\bar{h}}{12\omega^2\bar{\omega}} \left[\frac{(\bar{\omega} - \omega)(\bar{\omega} - 2\omega)}{(\omega + \bar{\omega})(\bar{\omega} + 2\omega)} \cos[(\bar{\omega} + 2\omega)t + \bar{\phi} + 2\phi] + \frac{(5\bar{\omega} + 11\omega)}{(\omega + \bar{\omega})} \cos(\bar{\omega}t + \bar{\phi}) \right. \\ &\quad \left. + \frac{4(\omega + \bar{\omega})}{(\bar{\omega} - 2\omega)} \cos[(2\omega - \bar{\omega})t + 2\phi - \bar{\phi}] \right] i\gamma_x \gamma_y, \end{aligned} \quad (12)$$

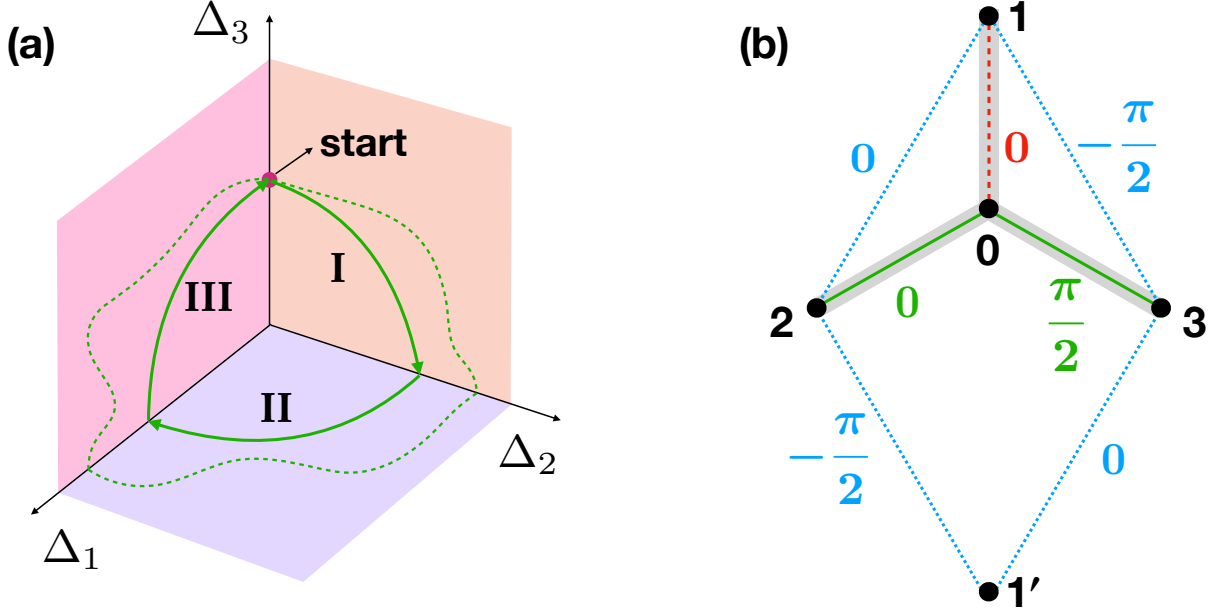


FIG. 4. (a) The solid green curve is one possible path for braiding in the parameter space of Δ_1 , Δ_2 and Δ_3 which subtends a solid angle of $\pi/2$ at the origin. A smooth deformation of the each path segment within the corresponding plane (shown as dashed green line) still subtends the same solid angle. (b) The basic setup containing three wires (gray segments) meeting at a junction with Majorana operators 1, 2, 3 at the ends and 0 at the junction. An additional operator 1' is placed for reasons explained in the text. Like before, the dashed red and dotted blue lines correspond to drives with frequencies $\bar{\omega}$ and ω respectively, and with respective phases shown. The solid green lines represent the effective low frequency couplings. The relative phases tell us this represents step I of the path of our protocol.

$$\mathcal{S}^{(4)}(t) = \frac{\hbar\hbar}{24(\omega + \bar{\omega})} \left[\left(\frac{\hbar^2(6\bar{\omega} - \omega)(\omega + \bar{\omega})^2 \cos[(\omega - 3\bar{\omega})t + \phi - 3\bar{\phi}]}{\omega\bar{\omega}^3(3\bar{\omega} - \omega)(2\bar{\omega} - \omega)} - \frac{\hbar^2(6\omega - \bar{\omega})(\omega + \bar{\omega})^2 \cos[(\bar{\omega} - 3\omega)t + \bar{\phi} - 3\phi]}{\omega^3\bar{\omega}(3\omega - \bar{\omega})(2\omega - \bar{\omega})} \right) \right. \\ \left. - \left(\frac{\hbar^2(\omega^2 + 7\omega\bar{\omega} + 22\bar{\omega}^2) \cos[(\omega + \bar{\omega})t + \phi + \bar{\phi}]}{\omega\bar{\omega}^3(\omega + 2\bar{\omega})} - \frac{\hbar^2(\bar{\omega}^2 + 7\omega\bar{\omega} + 22\omega^2) \cos[(\omega + \bar{\omega})t + \phi + \bar{\phi}]}{\omega^3\bar{\omega}(\bar{\omega} + 2\omega)} \right) \right. \\ \left. + \left(\frac{2\hbar^2(\bar{\omega} - \omega) \cos[(\omega + 3\bar{\omega})t + \phi + 3\bar{\phi}]}{\bar{\omega}^2(\omega + 2\bar{\omega})(\omega + 3\bar{\omega})} - \frac{2\hbar^2(\omega - \bar{\omega}) \cos[(\bar{\omega} + 3\omega)t + \bar{\phi} + 3\phi]}{\omega^2(\bar{\omega} + 2\omega)(3\omega + \bar{\omega})} \right) \right] i\gamma_y\gamma_z. \quad (13)$$

$$\mathcal{H}^{(3)}(t) = \frac{\hbar\hbar}{12\omega\bar{\omega}} \left[\frac{\hbar^2(10\omega^3 + 2\omega^2\bar{\omega} - \omega\bar{\omega}^2 + \bar{\omega}^3)}{\omega^2(\omega + \bar{\omega})(2\omega - \bar{\omega})} + \frac{\hbar^2(10\bar{\omega}^3 + 2\bar{\omega}^2\omega - \bar{\omega}\omega^2 + \omega^3)}{\bar{\omega}^2(\omega + \bar{\omega})(2\bar{\omega} - \omega)} \right] \sin(\Delta\omega t + \Delta\phi) i\gamma_y\gamma_z, \quad (14)$$

No contributions to braiding error at higher orders

At the leading order, we can see that the criteria for protection described in the main text are satisfied in our protocol. Now, we shall argue that even at higher orders, these criteria are still satisfied. For this, we just have to know the form of Δ_i in \mathcal{H} at all orders. A similar question was answered in the main text in the simpler case of three Majorana operators in the building block. We repeat the argument here for completeness. We know that $\mathcal{H}^{(n)}$ is non-zero only for odd n . At order $2p + 1$ (p is non-negative integer), $\mathcal{H}^{(2p+1)}$ is a product of terms $\sim (\gamma_x\gamma_y)^k (\gamma_x\gamma_z)^{2p+2-k} \sim \gamma_y^k \gamma_z^{2p+2-k}$, where we have used $\gamma_x^2 = 1$. This is either $\sim \gamma_y\gamma_z$ for odd k or ~ 1 for even k . The Clifford algebra of the Majorana operators, $\{\gamma_\alpha, \gamma_\beta\} = 2\delta_{\alpha\beta}$ and $\gamma_\alpha^\dagger = \gamma_\alpha$ for $\alpha, \beta = x, y, z$,

leads to a closed $\mathfrak{so}(3)$ algebra of the bilinears $\gamma_\alpha\gamma_\beta$, with $\alpha \neq \beta$. This, together with the nested commutator form in Eq. 2 in the main text, implies that identity 1 does not appear in this expansion, i.e., only odd k terms appear and hence all the terms in the effective Hamiltonian obtained at different orders of high frequency expansion are proportional to $\gamma_y\gamma_z$. Moreover, at higher orders, the only terms in \mathcal{H} are $\sim \sin[k(\Delta\omega t + \Delta\phi)]$ with odd k because, as explained above, only odd k terms appear in the series expansion of \mathcal{H} . There are no terms $\sim \cos[k(\Delta\omega t + \Delta\phi)]$ because in the limit $\omega \rightarrow \bar{\omega}$ and $\phi \rightarrow \bar{\phi}$, the nested commutator in Eq. 2 in the main text forces \mathcal{H} to 0. These facts can be verified up to $\mathcal{O}(\hbar^4/\omega^3)$ by the expressions for $\mathcal{H}^{(1)}$ and $\mathcal{H}^{(3)}$ in Eq. 10 and Eq. 14 respectively.

Let us now give a similar argument for segment I of

Fig. 4(a) which is a reproduction of Fig. 2(a) in the main text. We expect the effective Hamiltonian to be of the form $\Delta_2 i\gamma_0\gamma_2 + \Delta_3 i\gamma_0\gamma_3$, where Δ_2 starts from 0 and reaches a finite value while Δ_3 starts from a finite value and goes to 0 to satisfy the criteria. It follows from the nested commutator in Eq. 2 in the main text that, at any order in \mathcal{H} , the generic coupling of $\gamma_0\gamma_2$ comes from

$$\begin{aligned} &\sim (\gamma_0\gamma_1)^{k_1}(\gamma_1\gamma_2)^{k_2}(\gamma_3\gamma_1)^{k_3}(\gamma_{1'}\gamma_2)^{k_4}(\gamma_3\gamma_{1'})^{k_5} \\ &\sim \gamma_0^{k_1}\gamma_1^{k_1+k_2+k_3}\gamma_2^{k_2+k_4}\gamma_3^{k_3+k_5}\gamma_{1'}^{k_4+k_5}, \end{aligned}$$

where k_1, k_2, k_3, k_4 and k_5 are non-negative integers such that $k_1 + k_2 + k_3 + k_4 + k_5$ is even because $\mathcal{H}^{(n)}$ is non-zero only for odd n . The above form comes from the five drive terms shown as dashed red and dotted blue arrows in Fig. 4(b) which is a reproduction of Fig. 2(b) in the main text. Clearly, to get a $\gamma_0\gamma_2$ term, we need k_1 and $k_2 + k_4$ to be odd, and $k_1 + k_2 + k_3, k_3 + k_5$ and $k_4 + k_5$ to be even. This immediately implies that $k_3 + k_4$ is even, i.e., the drive terms with a relative phase of $\pi/2$ ($\gamma_3\gamma_1$ and $\gamma_{1'}\gamma_2$ terms) appear even number of times. Hence, the phase of the coupling of $\gamma_0\gamma_2$ is always a multiple of π . On the other hand, a similar analysis for $\gamma_0\gamma_3$ shows that the drive terms with a relative phase of $\pi/2$ appear odd number of times. Hence, the phase of the coupling of $\gamma_0\gamma_3$ is always an odd multiple of $\pi/2$. Therefore, $\Delta_2 \sim \sin(k\Delta\omega t + \text{“even”}\pi/2) \sim \sin(k\Delta\omega t)$, where k is odd because k_1 above is odd, and similarly, $\Delta_3 \sim \sin(k\Delta\omega t + \text{“odd”}\pi/2) \sim \cos(k\Delta\omega t)$, where k is odd. These forms ensure that Δ_3 starts from a finite value at $t = 0$ and goes to 0 at $t = \pi/2\Delta\omega$ while Δ_2 starts from 0 at $t = 0$ and reaches a finite value at $t = \pi/2\Delta\omega$, thereby satisfying the criteria mentioned in the main text for protection.

[1] J. M. Leinaas and J. Myrheim, *Il Nuovo Cimento B* (1971-1996) **37**, 1 (1977).
[2] F. Wilczek, *Phys. Rev. Lett.* **49**, 957 (1982).
[3] C. Nayak, S. H. Simon, A. Stern, M. Freedman, and S. Das Sarma, *Rev. Mod. Phys.* **80**, 1083 (2008).
[4] B. I. Halperin, *Phys. Rev. Lett.* **52**, 1583 (1984).
[5] D. Arovas, J. R. Schrieffer, and F. Wilczek, *Phys. Rev. Lett.* **53**, 722 (1984).
[6] D. A. Ivanov, *Phys. Rev. Lett.* **86**, 268 (2001).
[7] P. W. Shor, Fault-tolerant quantum computation, in *Proceedings of 37th Conference on Foundations of Computer Science*, pages 56–65, 1996.

[8] J. Preskill, *Proceedings of the Royal Society of London A: Mathematical, Physical and Engineering Sciences* **454**, 385 (1998).
[9] A. Kitaev, *Annals of Physics* **303**, 2 (2003).
[10] N. Read and D. Green, *Phys. Rev. B* **61**, 10267 (2000).
[11] G. Moore and N. Read, *Nuclear Physics B* **360**, 362 (1991).
[12] Y. Oreg, G. Refael, and F. von Oppen, *Phys. Rev. Lett.* **105**, 177002 (2010).
[13] R. M. Lutchyn, J. D. Sau, and S. Das Sarma, *Phys. Rev. Lett.* **105**, 077001 (2010).
[14] J. D. Sau, R. M. Lutchyn, S. Tewari, and S. Das Sarma, *Phys. Rev. Lett.* **104**, 040502 (2010).
[15] J. Alicea, *Phys. Rev. B* **81**, 125318 (2010).
[16] T. D. Stanescu, R. M. Lutchyn, and S. Das Sarma, *Phys. Rev. B* **84**, 144522 (2011).
[17] S. D. Sarma, M. Freedman, and C. Nayak, **1**, 15001 EP (2015).
[18] J. Shabani et al., *Phys. Rev. B* **93**, 155402 (2016).
[19] H. J. Suominen et al., *Phys. Rev. Lett.* **119**, 176805 (2017).
[20] V. Mourik et al., *Science* **336**, 1003 (2012).
[21] A. Das et al., *Nature Physics* **8**, 887 EP (2012).
[22] M. T. Deng et al., *Nano Letters* **12**, 6414 (2012), PMID: 23181691.
[23] H. O. H. Churchill et al., *Phys. Rev. B* **87**, 241401 (2013).
[24] A. D. K. Finck, D. J. Van Harlingen, P. K. Mohseni, K. Jung, and X. Li, *Phys. Rev. Lett.* **110**, 126406 (2013).
[25] H. Zhang et al., arXiv:1603.04069 (2016).
[26] M. T. Deng et al., *Science* **354**, 1557 (2016).
[27] M. T. Deng et al., *Science* **354**, 1557 (2016).
[28] J. Chen et al., *Science Advances* **3** (2017).
[29] H. Zhang et al., arXiv:1710.10701 (2017).
[30] A. Y. Kitaev, *Physics-Uspekhi* **44**, 131 (2001).
[31] S. M. Albrecht et al., *Nature* **531**, 206 (2016).
[32] M. Hell, K. Flensberg, and M. Leijnse, *Phys. Rev. B* **96**, 035444 (2017).
[33] L. Jiang et al., *Phys. Rev. Lett.* **106**, 220402 (2011).
[34] C. V. Kraus, P. Zoller, and M. A. Baranov, *Phys. Rev. Lett.* **111**, 203001 (2013).
[35] B. van Heck, A. R. Akhmerov, F. Hassler, M. Burrello, and C. W. J. Beenakker, *New Journal of Physics* **14**, 035019 (2012).
[36] J. Alicea, Y. Oreg, G. Refael, F. von Oppen, and M. P. A. Fisher, *Nat Phys* **7**, 412 (2011).
[37] J. D. Sau, D. J. Clarke, and S. Tewari, *Phys. Rev. B* **84**, 094505 (2011).
[38] T. Karzig, F. Pientka, G. Refael, and F. von Oppen, *Phys. Rev. B* **91**, 201102 (2015).
[39] T. Karzig et al., *Phys. Rev. B* **95**, 235305 (2017).
[40] In practice, all the drives have a finite bandwidth. For $\Delta\omega \sim 50$ MHz, a bandwidth of ~ 1 MHz is easily attainable.
[41] T. Karzig, Y. Oreg, G. Refael, and M. H. Freedman, *Phys. Rev. X* **6**, 031019 (2016).
[42] K. Flensberg, *Phys. Rev. Lett.* **106**, 090503 (2011).